

# Journal of Materials Chemistry A

Accepted Manuscript



This article can be cited before page numbers have been issued, to do this please use: C. Fu, A. Mahadevegowda and P. Grant, *J. Mater. Chem. A*, 2015, DOI: 10.1039/C5TA02210J.



This is an *Accepted Manuscript*, which has been through the Royal Society of Chemistry peer review process and has been accepted for publication.

*Accepted Manuscripts* are published online shortly after acceptance, before technical editing, formatting and proof reading. Using this free service, authors can make their results available to the community, in citable form, before we publish the edited article. We will replace this *Accepted Manuscript* with the edited and formatted *Advance Article* as soon as it is available.

You can find more information about *Accepted Manuscripts* in the [Information for Authors](#).

Please note that technical editing may introduce minor changes to the text and/or graphics, which may alter content. The journal's standard [Terms & Conditions](#) and the [Ethical guidelines](#) still apply. In no event shall the Royal Society of Chemistry be held responsible for any errors or omissions in this *Accepted Manuscript* or any consequences arising from the use of any information it contains.

# Fe<sub>3</sub>O<sub>4</sub>/Carbon Nanofibres with Necklace Architecture for Enhanced Electrochemical Energy Storage

Chaopeng Fu,\* Amoghavarsha Mahadevegowda, Patrick S. Grant

Department of Materials, University of Oxford, Oxford, United Kingdom, OX1 3PH.

\* E-mail: chaopeng.fu@materials.ox.ac.uk

## Abstract

Fe<sub>3</sub>O<sub>4</sub> spherulites on carbon nanofibres (CNF) to form novel necklace structures have been synthesised using a facile and scalable hydrothermal method, and their morphology and structure have been characterized using a range of electron microscopy and other techniques. The formation mechanism for the necklace structure has been proposed. The Fe<sub>3</sub>O<sub>4</sub>/CNF necklaces were sprayed onto large area current collectors to form electrodes with no binder and then investigated for their potential in supercapacitor and Li-ion battery applications. Supercapacitor electrodes in an aqueous KOH electrolyte delivered a high capacitance of 225 F g<sup>-1</sup> at 1 A g<sup>-1</sup> and Li-ion battery electrodes delivered a reversible capacity of over 900 mAh g<sup>-1</sup> at 0.05 C, and there was good cycling stability and rate capability in both configurations. When compared with the reduced performance of mixtures of the same materials without the necklace morphology, the enhanced performance can be ascribed to the robust, high mechanical stability and open scaffold structure in the necklace electrode that provides high ion mobility, while the percolating CNFs ensure low resistance electrical connection pathways to every electroactive Fe<sub>3</sub>O<sub>4</sub> spherulite to maximize storage behavior.

**Keywords:** iron oxides, carbon nanofibres, supercapacitor, Li ion battery

## Introduction

Concerns surrounding increasing environmental pollution and effects on climate change mandate increasing use of renewable and sustainable energy conversion technologies, which can be made more attractive by the use of efficient and safe electrical storage. Amongst the various energy conversion and storage technologies, supercapacitors and Li-ion batteries (LIBs) make use of electrochemical reactions to store electrical charge and have secured wide applications in portable electronics and electric vehicles.<sup>1-6</sup>

Supercapacitors, also called electrochemical capacitors, are energy storage devices that have high power density, long cycle life, high cycling efficiency, and operate by storing electrical charge through ion adsorption/desorption at an electrode/electrolyte interface and/or through fast surface redox reactions.<sup>1, 7, 8</sup> The electrodes in a supercapacitor may be electrochemically identical because adsorption/desorption reactions, and the electric double layer that is formed, do not necessarily involve any physical changes. In contrast, LIBs have much higher energy density and store electrical energy through lithiation/delithiation reactions at electrochemically dissimilar anodes and cathodes.<sup>4, 9</sup>

Despite the relative maturity of supercapacitors and LIBs, the growing market for portable electronics and electric vehicles and in particular the desire for the decarbonisation of electricity supplies provides new opportunities for these devices. While further improvements in power and energy densities of supercapacitor and LIBs system will always be valuable, there

is also a need for more carefully optimised balances of capacity, cycle life, calendar life, cost and safety depending on the application. Carbon-based materials dominate the commercial implementation in LIB anodes and supercapacitor electrodes that operate using organic solvent based electrolytes, but it is not clear that despite their relatively maturity, they always offer the best mix of properties, particularly for grid-scale and other emerging applications.

In the past few years, transition metal oxides have become intensively studied as electrode materials for both supercapacitors and LIBs. Transition metal oxides as supercapacitor electrodes have higher theoretical capacitance than carbon materials because additional surface specific redox reactions, alongside electric double layer capacitance, can be exploited.  $\text{MnO}_2$ ,  $\text{Co}_3\text{O}_4$ ,  $\text{NiO}$  and others with contrived and novel nanostructures have been investigated and have shown very high capacitances of up to  $1000 \text{ F g}^{-1}$ , compared with  $100\text{--}200 \text{ F g}^{-1}$  for “conventional” carbons.<sup>10–12</sup> Similarly, transition metal oxides as battery anodes, such as  $\text{Co}_3\text{O}_4$ ,  $\text{TiO}_2$ , etc., have also shown the potential for larger capacities than commercial graphite anodes. Unfortunately, in both applications metal oxides generally suffer from poor capacity retention resulting from pulverizing redox and intercalation reactions during cycling.<sup>13, 14</sup> Moreover, the relatively low conductivity of metal oxides can limit their rate capability, and their contrived nanostructures rely on synthesis routes that may be difficult to scale up.

Addressing these limitations and realising the potential benefits of metal oxides while avoiding, or at least restricting inherent disadvantages, requires a strategy to carefully design more suitable fine-scale arrangements of the constituent electrode materials to enable high power

and energy densities and long cycle life. A key challenge is to achieve a design-led or “structured” electrode using a combination of materials and processes that have potential to approach the comparatively low cost and very high productivity of currently used slurry cast electrodes. Arguably, current practical supercapacitor and LIB electrode materials and device arrangements are constrained primarily to those that are “drop-in” capable for current slurry casting practices. For example, three-dimensional  $\text{Co}_3\text{O}_4/\text{MnO}_2$  hierarchical nano-needle arrays on Ni foam showed promising performance as both supercapacitor and battery electrodes,<sup>15</sup> while mesoporous  $\text{NiCo}_2\text{O}_4$  nanowire arrays grown on carbon textiles again showed high specific capacity/capacitance using a rational, designed-led approach to the final architectures.<sup>16</sup> Although these and other metal oxides exhibited good laboratory performance, the relatively high cost, complicated synthesis and non-scalable processing restricts their full potential in technological implementations.

Recently, iron oxides have attracted attention as electrode materials for energy storage due to their abundance in nature, low cost and environmental benignity.<sup>17-20</sup> Meanwhile, commercially mature carbon nanofibres (CNFs) have also received interest in electrochemical energy storage systems because when mixed into an electrode their high aspect ratio and good electrical conductivity efficiently percolate electrical current at low fraction. CNFs are cheaper than carbon nanotubes which are often used similarly, and they also offer high mechanical and electrochemical stability.

In this paper we describe a facile method to fabricate crystalline  $\text{Fe}_3\text{O}_4$  spherulites regularly strung along CNFs to form a necklace structure. Our rationale is that firstly the CNFs are chosen to ensure the flow of electrons along the “strings” of the necklace, electron percolation through the electrode, and to the current collector; the CNFs also ensure a tangled, open but mechanically robust scaffold structure without need for binders. Secondly, the  $\text{Fe}_3\text{O}_4$  “beads” are then grown on the CNFs with dimensions  $< 300$  nm to ensure high surface area and good strain tolerance. Because every bead is threaded on a conducting CNF string through its centre, the full capacity of the  $\text{Fe}_3\text{O}_4$  can be exploited. A suspension of the necklaces are spray deposited onto large area current collectors (15 cm x 15 cm, shown in Figure S1) to form electrodes of thickness  $\sim 35$   $\mu\text{m}$  and mass loadings of 1.2 - 1.5  $\text{mg cm}^{-2}$ . The electrodes are shown to offer strong potential for both aqueous supercapacitor applications and organic electrolyte based LIB anodes, which is rationalised in terms of the necklace structure that facilitates both efficient electron and ion mobility, and good strain tolerance.

## Experimental and methods

### Synthesis of $\text{Fe}_3\text{O}_4$ /CNF composite materials

The CNFs were firstly activated by being refluxed in a concentrated nitric acid at 80 °C with constant stirring for 8h. The resulting suspension was diluted and rinsed with deionized water several times until the pH value was almost neutral. The resulting CNFs were separated from solution and dried in a vacuum oven. In a typical synthetic procedure, 3.25 g iron chloride and 0.15 g of these activated CNFs were added into 80 mL ethylene glycol, and the mixture stirred for 2h. The suspension was transferred into a Teflon-lined autoclave and the reaction

temperature was maintained at 200 °C for 16h. After being cooled down to room temperature naturally, the resulting black precipitates were washed with deionized water and ethanol several times by centrifuging and then dried in a vacuum oven at 80 °C overnight. For comparison, Fe<sub>3</sub>O<sub>4</sub> was also synthesized in the absence of CNFs under the same conditions.

### Materials characterization

Scanning electron microscopy images were obtained in a JEOL JSM-6500F. While transmission electron microscopy (TEM) and high resolution (HR)-TEM observations were performed in a field emission gun JEOL 3000F at an operating voltage of 300 kV. X-ray diffraction was conducted in a Siemens D-5000 powder diffractometer with 2θ step size of 0.05°. X-ray photoelectron spectroscopy spectra were obtained in a K-Alpha Fisher Scientific system with an Al X-ray source. Raman spectra were obtained using a Horiba LabRAM ARAMIS equipped with a 532 nm laser source. Thermogravimetric analysis to assess the relative proportion of carbon and iron oxide in the electrodes was conducted in a Perkin Elmer TG/DTA 6300. The mass of spray-deposited materials was measured by weighting the substrates before and after spraying using a Sartorius microbalance with 0.01 mg readability.

### Electrode fabrication

Working electrodes were coated using our novel spray processing equipment described elsewhere.<sup>21</sup> Briefly, the as-prepared powder materials and carbon black with a mass ratio of 90:10 were suspended into a water/ethanol mixture with a volume ratio of 1:1. The obtained suspension was sonicated for 15 minutes using a high power probe sonicator (Sonics and Materials Vibra Cell VC750). Subsequently, the well-dispersed suspensions were sprayed onto

stainless steel (SS) current collectors attached to a combined vacuum chuck and hotplate from a height of 10 cm. The mass loading and thickness were controlled at  $\sim 1.5 \text{ mg/cm}^2$  and  $\sim 35 \text{ }\mu\text{m}$  respectively (a typical as-sprayed thickness profile is shown in Figure S2).

### Electrochemical testing

Supercapacitor testing in 3M KOH aqueous solution at room temperature was conducted in a three-electrode cell using a Pt sheet as counter electrode, a Ag/AgCl reference electrode and a Gamry Ref 600 potentiostat. The inert behaviour of the substrate material alone in the electrolyte was confirmed by cyclic voltammetry. This electrolyte concentration was chosen as it has previously provided good performance with iron oxides, and 3M (rather than 1M which is also well-studied) helps to minimize the possibility of hydrogen evolution.<sup>22-27</sup> Electrochemical impedance spectroscopy was performed in the frequency range 100 kHz to 0.01 Hz at the open potential with a potential amplitude of 5 mV.

For battery testing, electrodes were obtained similarly as the supercapacitor electrodes, except the suspension for spraying now composed carbon black and CMC binder with a mass ratio of 80:10:10 and using copper foil as the substrate/current collector. The sprayed electrodes were gently calendered by hand using a polished Al cylinder and dried under vacuum at 100 °C overnight. 2032-type coin cells were assembled in an Ar-filled glovebox using Li metal sheet as the counter electrode. The electrolyte was 1 M LiPF<sub>6</sub> dissolved in a mixture of ethylene carbonate (EC) and diethylene carbonate (DEC) with a volume ratio of 1:1. Galvanostatic



charge/discharge testing was performed using an Arbin battery test system (Arbin BT-G-25) in a voltage window of 0.05-3 V vs Li/Li<sup>+</sup> at various currents.

## Results and discussion

### Morphology and structure

The scanning electron microscopy (SEM) image in Figure 1a displays the Fe<sub>3</sub>O<sub>4</sub> bead-on-CNF string structure with the Fe<sub>3</sub>O<sub>4</sub> beads threaded onto the CNFs. The transmission electron microscopy (TEM) image in Figure 1b shows Fe<sub>3</sub>O<sub>4</sub> diameters of ~300 nm, and carbon nanofibres diameters of ~100 nm and lengths of several hundred μm. Figure 1c shows a high resolution TEM (HRTEM) image taken from the edge of a single bead in Figure 1b, where the lattice spacings were calculated from the image as 0.488 nm and 0.298 nm, which matched closely to the (111) and (220) spacing of cubic Fe<sub>3</sub>O<sub>4</sub>.<sup>28-30</sup> The selected area electron diffraction (SAED) pattern in Figure 1d displays a second ring indexed to the (002) plane of the CNF,<sup>31</sup> and all other rings were readily indexed to cubic Fe<sub>3</sub>O<sub>4</sub>. There was no evidence for the presence of any minority Fe<sub>2</sub>O<sub>3</sub> or surface FeOOH, as sometimes may be present on Fe<sub>3</sub>O<sub>4</sub>.<sup>32</sup>

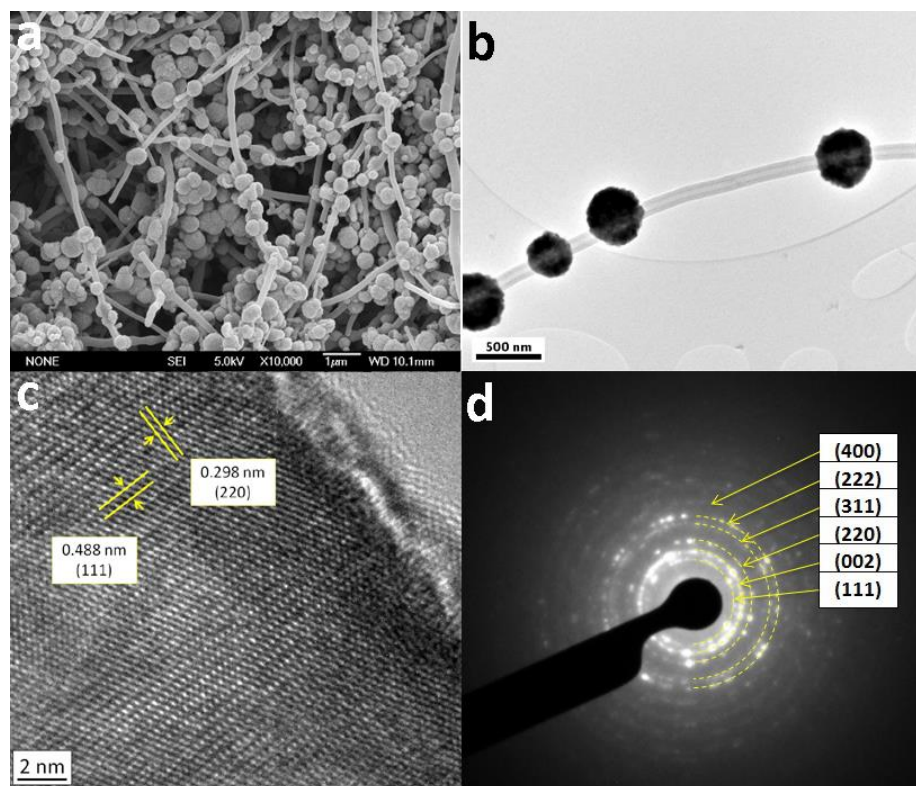


Figure 1 (a, b) SEM and TEM images of the as-prepared  $\text{Fe}_3\text{O}_4/\text{CNF}$  necklaces respectively, (c,d) HRTEM image and SAED pattern from the  $\text{Fe}_3\text{O}_4$  bead respectively.

Figure 2a shows XRD patterns from the  $\text{Fe}_3\text{O}_4/\text{CNF}$  necklaces and the superimposed diffraction peaks from the JCPDS reference 00-019-0629 for  $\text{Fe}_3\text{O}_4$ , confirming the presence of crystalline  $\text{Fe}_3\text{O}_4$  only. The sharp peaks indicated a high degree of crystallinity with the broad peak at  $26.2^\circ$  ascribed to the (002) peak of the CNF. X-ray photoelectron spectroscopy (XPS) was used to characterize more carefully the surface chemistry and structure of the pristine  $\text{Fe}_3\text{O}_4/\text{CNF}$  necklaces, as shown in Figure 2b. Two main peaks accompanied by their satellite peaks between 705 and 735 eV were resolved at 724.6 eV and 711.0 eV, which were assigned to Fe  $2p_{1/2}$  and Fe  $2p_{3/2}$  respectively, and were again consistent with the standard  $\text{Fe}_3\text{O}_4$  XPS

spectrum.<sup>33, 34</sup> Figure 2c shows a detailed scan of the binding energy spectrum in the region of carbon species. There were binding energies at 284.5 eV, 285.6 eV and 288.7 eV which corresponded to C-C, C-O, and O-C=O bonds respectively.<sup>35, 36</sup> The generation of oxygen-containing functional groups on the CNFs was due to CNF surface oxidation during the chemical activation step used to facilitate the formation the bead-on-string structure, as described later.

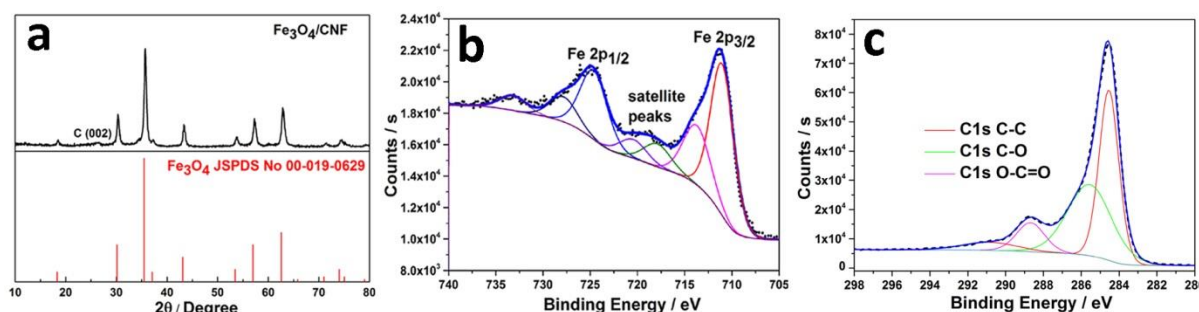


Figure 2 (a) XRD patterns, (b) the Fe 2p XPS spectrum, and (c) the C1s XPS spectrum of  $\text{Fe}_3\text{O}_4/\text{CNF}$  necklaces

Figure 3a shows the Raman spectrum of pristine  $\text{Fe}_3\text{O}_4/\text{CNF}$  with the two peaks at  $494\text{ cm}^{-1}$  and  $706\text{ cm}^{-1}$  corresponding to the  $\text{T}_{2g}$  and  $\text{A}_{1g}$  modes for  $\text{Fe}_3\text{O}_4$  respectively, again confirming  $\text{Fe}_3\text{O}_4$ .<sup>37, 38</sup> The typical D and G bands at frequencies of  $1363\text{ cm}^{-1}$  and  $1599\text{ cm}^{-1}$  relate to the CNFs.<sup>39</sup> Thermogravimetric analysis (TGA) was carried out in air to  $800\text{ }^\circ\text{C}$  to measure the  $\text{Fe}_3\text{O}_4$  fraction as the CNFs were oxidized to  $\text{CO}_2$ , and  $\text{Fe}_3\text{O}_4$  was oxidized to  $\text{Fe}_2\text{O}_3$ . According to weight percentage loss shown in Figure 3b and accounting for both C loss and  $\text{Fe}_3\text{O}_4$  to  $\text{Fe}_2\text{O}_3$  transformation, the original weight percentage of  $\text{Fe}_3\text{O}_4$  in the necklaces was estimated at  $\sim 86\%$ .

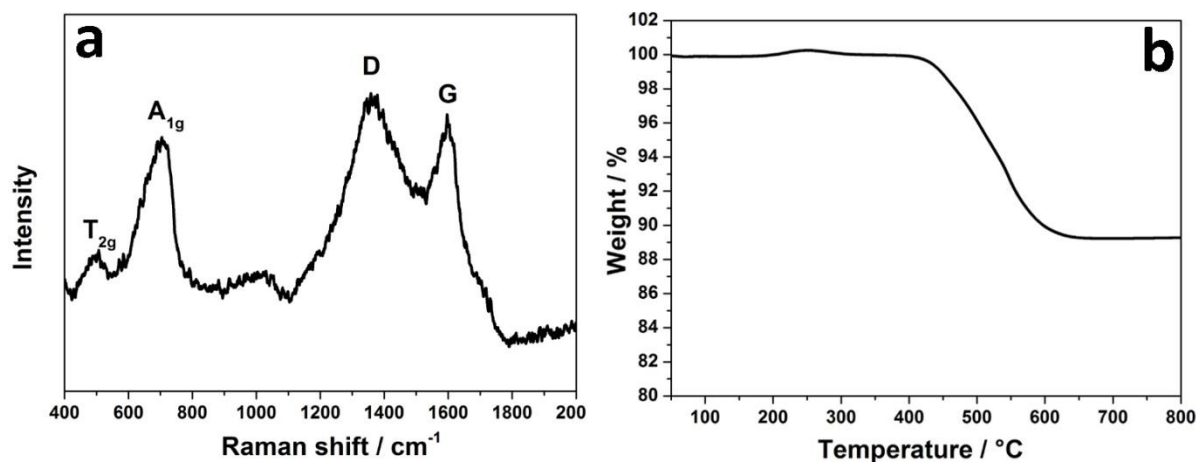


Figure 3 (a) Raman spectrum and (b) TGA profile of the Fe<sub>3</sub>O<sub>4</sub>/CNF necklaces.

To reveal the formation process of Fe<sub>3</sub>O<sub>4</sub>/CNF necklace, Figure S3 shows SEM images of how the necklace morphology developed by interrupting the hydrothermal process at 4, 8, 12 and 16 hr. At 4 hr, there were no Fe<sub>3</sub>O<sub>4</sub> beads and only a few very small particulates decorating some CNFs at the early stage of nucleation and growth, as shown in Figure S3a. After 8 hr, the CNFs became near-continuously covered in blocky particles and after 12 hr, the spherulite morphology began to emerge. After 16 hr in Figure S3d the fully formed crystalline Fe<sub>3</sub>O<sub>4</sub> beads were distinct. The proposed mechanism for the formation of the Fe<sub>3</sub>O<sub>4</sub>/CNF necklace structure is illustrated in Figure 4. At the first stage, when the CNFs were refluxed in strong acid, surface oxidation occurred resulting in the generation of oxygen-containing functional groups. The XPS data showed that the oxygen-containing functional groups included negatively charged carboxyl groups and hydroxyl groups that subsequently interact strongly with positively charged iron ions due to electrostatic interactions or covalent chemical bonding. Under the hydrothermal conditions, these bonded iron ions served subsequently as preferential centres for the

nucleation and growth of the discrete  $\text{Fe}_3\text{O}_4$  beads so that as the reaction proceeded, the anchored  $\text{Fe}_3\text{O}_4$  particles grew with intimate contact on the CNF surface, to aid electron transfer in electrochemical reactions.

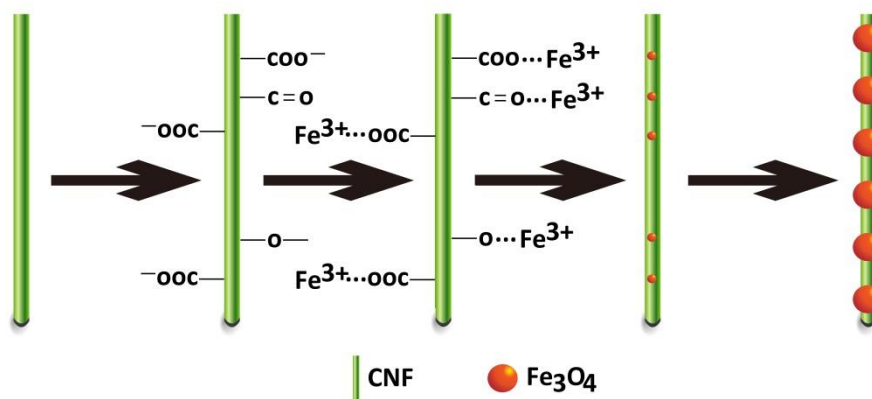


Figure 4 Schematic illustration of the proposed mechanism of formation of  $\text{Fe}_3\text{O}_4/\text{CNF}$  necklaces.

### Supercapacitor performance

The supercapacitor performance of the  $\text{Fe}_3\text{O}_4/\text{CNF}$  necklaces was evaluated by various electrochemical techniques. For comparison purpose,  $\text{Fe}_3\text{O}_4$  particles prepared similarly and of similar size were randomly mixed with CNFs in the same mass ratio (denoted as  $\text{Fe}_3\text{O}_4+\text{CNF}$ , SEM images shown in Figure S4) and then formed into similar thickness electrodes by the same spray deposition process under identical conditions. Figure 5a shows the cyclic voltammetry (CV) curves of the  $\text{Fe}_3\text{O}_4/\text{CNF}$  necklace and  $\text{Fe}_3\text{O}_4+\text{CNF}$  random mix electrodes in 3M KOH at a potential scan rate of  $25 \text{ mV s}^{-1}$ . The shape of both CV curves deviated from an ideal rectangular voltammogram associated with electric double layer capacitance only, indicating significant

pseudo-capacitive behaviour. A pair of very broad peaks was located at approximately -0.77 V resulting from the redox reaction of oxygen-containing functional groups on the CNFs. Additionally, there was another pair of redox peaks for both electrodes: an anodic peak located at approximately -0.90 V and a corresponding cathodic peak potential at approximately -0.98 V for the Fe<sub>3</sub>O<sub>4</sub>/CNF necklace electrode, and an anodic peak and a cathodic peak located at approximately -0.85 V and -0.98 V respectively for the Fe<sub>3</sub>O<sub>4</sub>+CNF electrode. These peaks were associated with the reversible surface reaction between Fe<sup>3+</sup> and Fe<sup>2+</sup> ( $\text{Fe}^{3+} + \text{e} \leftrightarrow \text{Fe}^{2+}$ ).<sup>22, 40</sup> The smaller peak potential separation of the Fe<sub>3</sub>O<sub>4</sub>/CNF necklace electrode indicated better reversibility.<sup>41, 42</sup> Moreover, the current density and integrated area bounded by the CV curve of the Fe<sub>3</sub>O<sub>4</sub>/CNF necklace electrode were much larger than Fe<sub>3</sub>O<sub>4</sub>+CNF electrode, inferring the more efficient utilization of the Fe<sub>3</sub>O<sub>4</sub> in this format since the electrodes were otherwise identical.

CV curves for the higher performing Fe<sub>3</sub>O<sub>4</sub>/CNF necklace electrode at a range of scan rates from 5 to 100 mV s<sup>-1</sup> are shown in Figure 5b. The CV curves retained their shape at all scan rates, suggesting sufficiently fast charge transfer kinetics and implying relatively high rate performance, which is often problematic in Fe<sub>3</sub>O<sub>4</sub>.<sup>43</sup>

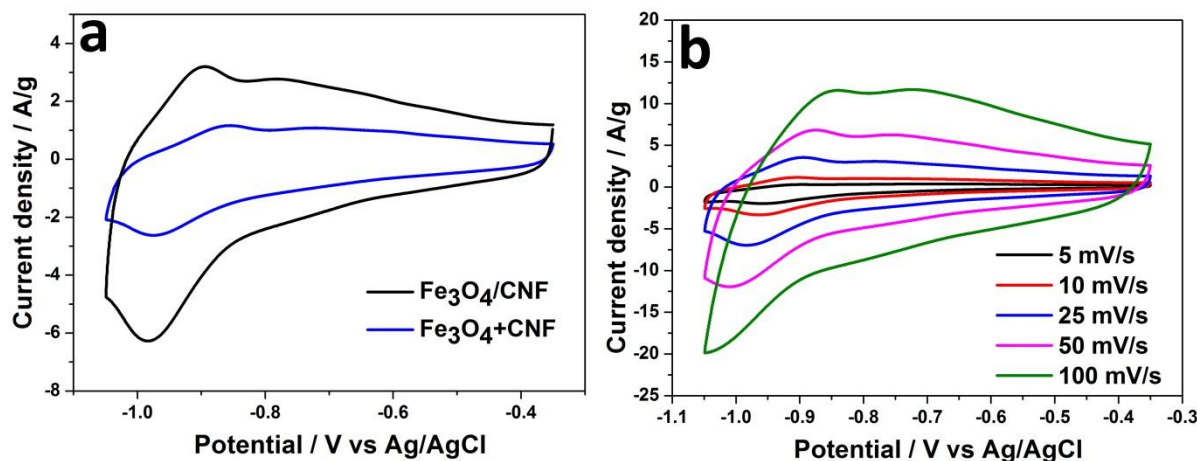


Figure 5 (a) CV curves of Fe<sub>3</sub>O<sub>4</sub>/CNF and Fe<sub>3</sub>O<sub>4</sub>+CNF electrodes in KOH at 25 mV s<sup>-1</sup>; and (b) CV curves of the Fe<sub>3</sub>O<sub>4</sub>/CNF necklace electrode at a range of scan rates from 5 mV s<sup>-1</sup> to 100 mV s<sup>-1</sup>.

Galvanostatic charge/discharge measurements were also conducted and discharge curves at current densities from 1 A g<sup>-1</sup> to 8 A g<sup>-1</sup> are shown in Figure 6a. The deviation from a straight line again showed the pseudocapacitive character of the storage reaction.<sup>44</sup> The specific capacitance  $C_{sp}$  was estimated using:<sup>45</sup>

$$C_{sp} = \frac{I}{dE/dt}$$

where  $I$  is the discharge current density in A g<sup>-1</sup>, and  $dE/dt$  is the slope of the discharge curve. The resulting specific capacitance as a function of current density is shown in Figure 6b. The Fe<sub>3</sub>O<sub>4</sub>/CNF necklace electrode exhibited at least two times higher specific capacitance than the Fe<sub>3</sub>O<sub>4</sub>+CNF electrode: for example, the specific capacitance of Fe<sub>3</sub>O<sub>4</sub>/CNF was 225 F g<sup>-1</sup> at 1 A g<sup>-1</sup>, which was retained at 106 F g<sup>-1</sup> when the current density increased to 10 A g<sup>-1</sup>; while the

$\text{Fe}_3\text{O}_4$ +CNF electrode had a specific capacity of  $107 \text{ F g}^{-1}$  at  $1 \text{ A g}^{-1}$ , reducing to only  $15 \text{ F g}^{-1}$  at  $10 \text{ A g}^{-1}$ .

Electrochemical impedance spectroscopy (EIS) was used to construct the Nyquist plot in Figure 6c, where in each plot, there was an approximate semi-circle in the high frequency region, followed by two near-linear sections at middle and low frequencies. In the high frequency region, the equivalent series resistance (ESR, intersection on the real axis at high frequency) and charge transfer resistance ( $R_{\text{ct}}$ , the diameter of the semi-circle) were estimated to be  $0.5 \Omega$  and  $3.0 \Omega$  respectively for the  $\text{Fe}_3\text{O}_4$ /CNF necklace electrode, and  $3.1 \Omega$  and  $22.0 \Omega$  respectively for the  $\text{Fe}_3\text{O}_4$ +CNF electrode. The smaller ESR indicated the higher electrical conductivity of the  $\text{Fe}_3\text{O}_4$ /CNF necklace electrode, and the smaller  $R_{\text{ct}}$  indicated its faster charge transfer capability.<sup>32</sup> At middle and low frequencies, the transition between the two regions is sometimes termed the “knee” frequency,<sup>46</sup> and denotes the highest frequency at which the electrode can exhibit capacitive behaviour, and is an indication of the power capability of a supercapacitor.<sup>47</sup> A knee frequency for the  $\text{Fe}_3\text{O}_4$ /CNF necklace electrode of  $38.4 \text{ Hz}$  was significantly higher than  $4.4 \text{ Hz}$  for the  $\text{Fe}_3\text{O}_4$ +CNF mixed electrode, again indicating better rate performance.

Long term cycling stability is a defining and key parameter for the practical application of a supercapacitor, and capacitance as a function of cycle number at  $1 \text{ A g}^{-1}$  is shown in Figure 6d. The  $\text{Fe}_3\text{O}_4$ /CNF necklace electrode retained 85% of its initial value after 2,000 cycles, while the capacitance of  $\text{Fe}_3\text{O}_4$ +CNF faded to 62%.



It is instructive to compare the performance of our Fe<sub>3</sub>O<sub>4</sub>/CNF necklace electrode with other similar work. Table S1 lists the specific capacitance and cycling performance of various Fe<sub>3</sub>O<sub>4</sub> based electrodes. Some of these configurations similarly make use of intimate contact between fine-scale Fe<sub>3</sub>O<sub>4</sub> and a carbon-based electron carrier. The supercapacitive performance of the Fe<sub>3</sub>O<sub>4</sub>/CNF necklaces is superior to many of the previous works, and it is noticeable that most previous work considered only low current densities, which tend to show pseudocapacitor performance in the best light. When current densities up to 10 A g<sup>-1</sup> are considered, the current work is only approached by Reference [4] in the ESI, but which involved an additional, inconvenient heat treatment of the Fe<sub>3</sub>O<sub>4</sub> at relatively high temperature.

The attractive performance of the Fe<sub>3</sub>O<sub>4</sub>/CNF necklaces of large capacitance, good rate performance and long cycling life is ascribed to the CNFs that form a tangled, open scaffold structure that ensures no aggregation of the Fe<sub>3</sub>O<sub>4</sub> spheres, which in turn ensures a high surface area to mass or volume ratio. The *in-situ* formation of the Fe<sub>3</sub>O<sub>4</sub> directly on the CNF as a substrate ensures good electron transfer for every Fe<sub>3</sub>O<sub>4</sub> sphere with no requirement for percolation of current between Fe<sub>3</sub>O<sub>4</sub> particles themselves. The decorated CNFs wet the current collector through the aqueous dispersion used in spray processing and again this ensures good electron transfer characteristics.

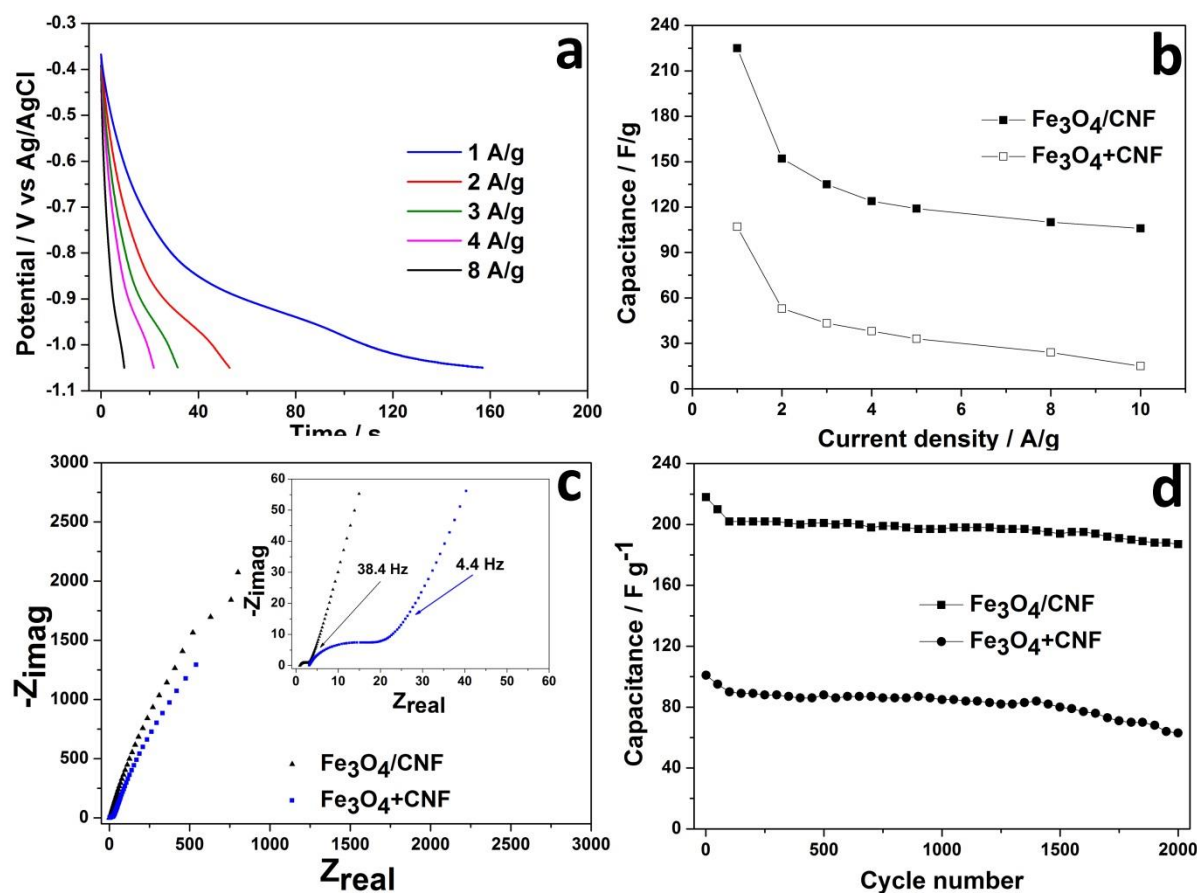
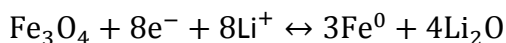


Figure 6 (a) Discharge curves of the  $\text{Fe}_3\text{O}_4/\text{CNF}$  necklace electrode at various discharge current densities; (b) specific capacitance as a function of current density for  $\text{Fe}_3\text{O}_4/\text{CNF}$  necklace and  $\text{Fe}_3\text{O}_4+\text{CNF}$  electrodes; (c) Nyquist plots with labelled knee frequencies; and (d) the specific capacitance as a function of cycle number for  $\text{Fe}_3\text{O}_4/\text{CNF}$  necklace and  $\text{Fe}_3\text{O}_4+\text{CNF}$  electrodes.

### Battery performance

$\text{Fe}_3\text{O}_4$  is a promising anode material for Li-ion batteries due to its high theoretical specific capacity of 924 mAh g<sup>-1</sup>, low cost, non-toxicity and environmental benignity,<sup>48</sup> and amongst metal oxides it has a comparatively high electrical conductivity of approximately 10<sup>4</sup> S cm<sup>-1</sup>.<sup>49</sup> The electrochemical reversible reaction of  $\text{Fe}_3\text{O}_4$  with Li<sup>+</sup> in LIBs can be summarized as:<sup>50, 51</sup>



Coin cell batteries were fabricated using the  $\text{Fe}_3\text{O}_4/\text{CNF}$  necklace electrodes, which were essentially identical to those used as supercapacitor electrodes and already described.

Figure 7a displays typical galvanostatic charge/discharge curves for the  $\text{Fe}_3\text{O}_4/\text{CNF}$  electrode between 0.05 V and 3.0 V versus  $\text{Li}/\text{Li}^+$  at a charge/discharge rate of 0.05 C (1C = 1000 mA/g). During the first discharging cycle, the voltage fell sharply to ~1.25 V, where there was a short voltage plateau that was attributed to the formation of  $\text{Li}_x\text{Fe}_2\text{O}_3$ , and then decreased again to ~0.6 V, where there was a more prolonged voltage plateau that was attributed to the complete conversion from  $\text{Li}_x\text{Fe}_2\text{O}_3$  to metallic  $\text{Fe}^0$ .<sup>52</sup> Then the voltage gradually reduced towards the cut-off voltage 0.05 V, which involved in the formation of the solid electrolyte interphase (SEI). This first discharge shows a high capacity of 1578 mAh  $\text{g}^{-1}$  because of the initial reduction of the electrolyte and the formation of the SEI layer. During the first charging process, the voltage rose gradually and there were again two voltage plateau, which were ascribed to the reversible oxidation of metallic Fe to  $\text{Fe}_3\text{O}_4$ . When the voltage reached 3 V, a charge capacity of 1068 mAh  $\text{g}^{-1}$  was achieved, leading to a first cycle Coulomb efficiency of 68% and a significant irreversible capacity loss, particularly related to the formation of the SEI layer on the  $\text{Fe}_3\text{O}_4$  and decomposition of electrolyte, which are frequently observed for most anodes.<sup>14, 48</sup> During the following cycles, the discharge curves kept a similar shape, but the voltage of the long plateau shifted upward to approximately 0.9 V, accompanied by a decrease in capacity but an increase in Coulombic efficiency. The specific capacity and Coulombic efficiency at 0.05 C as a function of

cycle number are shown in Figure 7b with capacity reduced primarily in the first 3 cycles only, and then remaining stable with a reversible capacity of 836 mAh g<sup>-1</sup> after 100 cycles. Correspondingly, the Coulombic efficiency rose from the first cycle value of 68% to 98% in the third cycle, and remained stable up to 100 cycles. Figure 7b also shows that the Fe<sub>3</sub>O<sub>4</sub>/CNF electrode showed good performance at a higher current density (1 C), with a retained specific capacity of 637 mAh g<sup>-1</sup> after 100 cycles, which was preceded by 3 cycles at 0.05 C.

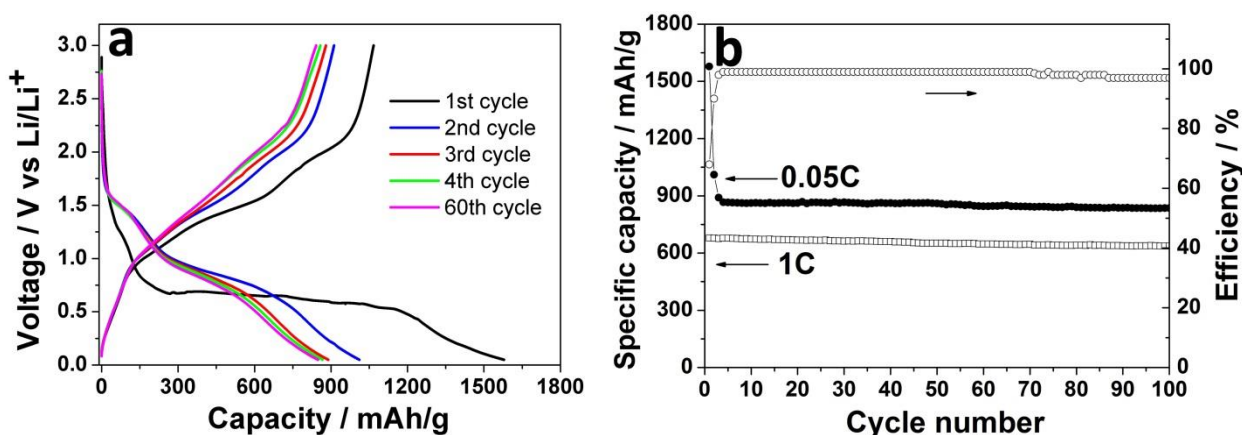


Figure 7 (a) Charge/discharge curves of the Fe<sub>3</sub>O<sub>4</sub>/CNF necklace electrode at 0.05C; and (b) specific capacity at 0.05 and 1 C and efficiency at 0.05 C as a function of cycle number.

Rate performance was also investigated in the same voltage window between 0.05 V and 3 V vs Li/Li<sup>+</sup>. As the charge/discharge curves in Figure 8a show, an increase in current density decreased the discharge voltage plateau, and the charge voltage plateau slightly increased rendering a higher over-potential, and the capacity reduced with increasing current density. The specific capacities at the various current densities of both Fe<sub>3</sub>O<sub>4</sub>/CNF necklace electrode and Fe<sub>3</sub>O<sub>4</sub>+CNF random mix electrode are shown in Figure 8b. The Fe<sub>3</sub>O<sub>4</sub>/CNF necklace electrode delivered a stable capacity of ~900 mAh g<sup>-1</sup> at 0.05C, 872 mAh g<sup>-1</sup> at 0.1C, 722 mAh g<sup>-1</sup>

at 0.5C, 667 mAh g<sup>-1</sup> at 1C, 523 mAh g<sup>-1</sup> at 5C, and was superior to an equivalent Fe<sub>3</sub>O<sub>4</sub>+CNF randomly mixed electrode at all discharge current densities. The capacity at 5C was larger than the theoretical capacity of commercial graphite anodes (372 mAh g<sup>-1</sup>), and when the current rate returned to 0.05 C again after 25 cycles, the capacity rebounded to approximately 870 mAh g<sup>-1</sup>, indicating the electrode structure was robust even at relatively fast charge/discharge rates. The microstructure of the Fe<sub>3</sub>O<sub>4</sub>/CNF electrode after 5 cycles at each of the C rates and 30 cycles in total was investigated in the TEM. Figure S5 shows a representative image indicating that while some degradation of the Fe<sub>3</sub>O<sub>4</sub> cannot be ruled out entirely, the spherulites and the necklace morphology were robust during cycling. Table S2 gives the performance of a range of high performing Fe<sub>3</sub>O<sub>4</sub> based anodes from the literatures where again in each case the Fe<sub>3</sub>O<sub>4</sub> was combined with a carbonaceous material to promote electrical conductivity. Similarly to the supercapacitor performance, the Fe<sub>3</sub>O<sub>4</sub>/CNF necklace electrode displayed one of the most promising specific capacity-rate and capability-cycle life combinations.

To further understand how the necklace structure contributed to this encouraging performance, EIS was conducted in the frequency range 100 kHz to 0.01 Hz. The Nyquist plots of both Fe<sub>3</sub>O<sub>4</sub>/CNF necklace and Fe<sub>3</sub>O<sub>4</sub>+CNF random mix electrodes are shown in Figure 8c. Similarly to the supercapacitor format, the smaller ESR (20 Ω versus 38 Ω) indicated the improved electrical conductivity of the Fe<sub>3</sub>O<sub>4</sub>/CNF electrode, and smaller charge transfer resistance (49 Ω versus 101 Ω) at the interface between electrode and electrolyte indicated a faster electron transfer capability of the Fe<sub>3</sub>O<sub>4</sub>/CNF electrode.<sup>53</sup>

Compared with the  $\text{Fe}_3\text{O}_4$ +CNF mixed electrode, the  $\text{Fe}_3\text{O}_4$ /CNF necklace electrode displayed improved battery performance with a higher capacity, longer cycle life and better rate capability, deriving from the robust architecture, and the characteristics already advocated for the superior supercapacitor performance. Firstly, all the  $\text{Fe}_3\text{O}_4$  spheres are attached on the CNF strings, avoiding high contact resistance and offering a continuous electron transport path, resulting in good rate performance. Secondly, the open CNF scaffold effectively prevents the aggregation of  $\text{Fe}_3\text{O}_4$  spheres; meanwhile,  $\text{Fe}_3\text{O}_4$  spheres to some extent can also prevent close-packing of CNFs. Lastly, the mechanically stable but flexible bead-on-string structure can accommodate the volume expansion/contraction of  $\text{Fe}_3\text{O}_4$  spheres during lithiation/delithiation cycles.

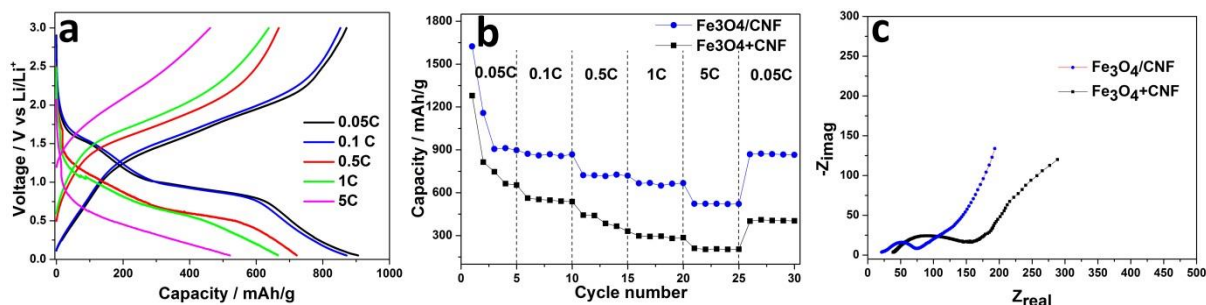


Figure 8 (a) Charge/discharge curves of the  $\text{Fe}_3\text{O}_4$ /CNF composite electrode at various rates, (b) Cycling performance at various rates and (c) Nyquist plots of the  $\text{Fe}_3\text{O}_4$ /CNF necklace and  $\text{Fe}_3\text{O}_4$ +CNF electrodes.

## Conclusions

$\text{Fe}_3\text{O}_4$  crystalline “beads” threaded on commercial CNF “strings” were successfully synthesized through a facile hydrothermal method with a  $\text{Fe}_3\text{O}_4$  weight fraction of approximately 86%.

These Fe<sub>3</sub>O<sub>4</sub>/CNF necklace materials were suspended in solution and then sprayed onto large area current collectors (15 cm x 15 cm) to form ~35 μm thick electrodes that were investigated for both supercapacitor and Li-ion battery applications. As a supercapacitor electrode, the Fe<sub>3</sub>O<sub>4</sub>/CNF showed a high specific capacitance of 225 F g<sup>-1</sup> at 1 A g<sup>-1</sup> in KOH electrolyte, which was retained at 85% after 2,000 cycles, and with good rate performance that provided 106 F g<sup>-1</sup> at 10 A g<sup>-1</sup>. As a Li-ion battery anode, the Fe<sub>3</sub>O<sub>4</sub>/CNF had a reversible capacity of over 900 mAh g<sup>-1</sup> at 0.05 C, retained at 845 mAh g<sup>-1</sup> after 60 cycles; and a good rate of performance of 523 mAh g<sup>-1</sup> at 5C. The supercapacitor and battery performance was superior to a random but otherwise identical mixture of Fe<sub>3</sub>O<sub>4</sub>+CNF in both electrode applications. The enhanced performance was ascribed to the designed bead-on-string architecture that provided ready electron transfer and percolation, an open scaffold for ion accessibility, nano-scale Fe<sub>3</sub>O<sub>4</sub> spheres with maximised area to volume ratio and good strain tolerance, and restricted agglomeration of either Fe<sub>3</sub>O<sub>4</sub> or CNF materials. The feedstock chemicals for the Fe<sub>3</sub>O<sub>4</sub> are relatively low cost compared with Ni and Co oxides, the hydrothermal route is relatively scaleable, the cost of CNFs is lower than commercial carbon nanotubes or graphene frequently used in other studies that also often use small-scale 3D substrates that cannot be scaled-up (see Table S1), while the spray deposition route has been demonstrated at meter length electrode scale already, with no particular restrictions for further scale-up.<sup>54</sup>

## Acknowledgements

The authors would like to thank the UK Engineering and Physical Sciences Research Council for financial support (Grant EP/K002252/1).

## References

1. P. Simon and Y. Gogotsi, *Nat. Mater.*, 2008, **7**, 845-854.
2. L. L. Zhang and X. S. Zhao, *Chem. Soc. Rev.*, 2009, **38**, 2520-2531.
3. P. G. Bruce, S. A. Freunberger, L. J. Hardwick and J. M. Tarascon, *Nat. Mater.*, 2012, **11**, 19-29.
4. M. G. Kim and J. Cho, *Adv. Funct. Mater.*, 2009, **19**, 1497-1514.
5. J. Speirs, M. Contestabile, Y. Houari and R. Gross, *Renew. Sustainable Energy Rev.*, 2014, **35**, 183-193.
6. J. M. Tarascon and M. Armand, *Nature*, 2001, **414**, 359-367.
7. X. W. Ma, J. W. Liu, C. Y. Liang, X. W. Gong and R. C. Che, *J. Mater. Chem. A*, 2014, **2**, 12692-12696.
8. R. T. Wang, X. B. Yan, J. W. Lang, Z. M. Zheng and P. Zhang, *J. Mater. Chem. A*, 2014, **2**, 12724-12732.
9. J. B. Goodenough and K.-S. Park, *J. Am. Chem. Soc.*, 2013, **135**, 1167-1176.
10. L. Li, Y. Q. Zhang, X. Y. Liu, S. J. Shi, X. Y. Zhao, H. Zhang, X. Ge, G. F. Cai, C. D. Gu, X. L. Wang and J. P. Tu, *Electrochim. Acta*, 2014, **116**, 467-474.
11. Y. Liu, W. Wang, Y. Wang, Y. Ying, L. Sun and X. Peng, *RSC Advances*, 2014, **4**, 16374-16379.
12. K. Xu, R. Zou, W. Li, Y. Xue, G. Song, Q. Liu, X. Liu and J. Hu, *J. Mater. Chem. A*, 2013, **1**, 9107-9113.
13. H. Sun, G. Xin, T. Hu, M. Yu, D. Shao, X. Sun and J. Lian, *Nat. Commun.*, 2014, **5**, 4526-4533.



14. M. Xu, F. Wang, Y. Zhang, S. Yang, M. Zhao and X. Song, *Nanoscale*, 2013, **5**, 8067-8072.
15. D. Kong, J. Luo, Y. Wang, W. Ren, T. Yu, Y. Luo, Y. Yang and C. Cheng, *Adv. Funct. Mater.*, 2014, **24**, 3815-3826.
16. L. Shen, Q. Che, H. Li and X. Zhang, *Adv. Funct. Mater.*, 2014, **24**, 2630-2637.
17. J. Mu, B. Chen, Z. Guo, M. Zhang, Z. Zhang, P. Zhang, C. Shao and Y. Liu, *Nanoscale*, 2011, **3**, 5034-5040.
18. J. M. Jeong, B. G. Choi, S. C. Lee, K. G. Lee, S. J. Chang, Y. K. Han, Y. B. Lee, H. U. Lee, S. Kwon, G. Lee, C.-S. Lee and Y. S. Huh, *Adv. Mater.*, 2013, **25**, 6250-6255.
19. X. Liu, W. Si, J. Zhang, X. Sun, J. Deng, S. Baunack, S. Oswald, L. Liu, C. Yan and O. G. Schmidt, *Sci. Rep.*, 2014, **4**, 7452-7459.
20. Y. Jiang, D. Zhang, Y. Li, T. Yuan, N. Bahlawane, C. Liang, W. Sun, Y. Lu and M. Yan, *Nano Energy*, 2014, **4**, 23-30.
21. X. Zhao, C. Hinchliffe, C. Johnston, P. J. Dobson and P. S. Grant, *Materials Science and Engineering: B*, 2008, **151**, 140-145.
22. P. M. Hallam, M. Gomez-Mingot, D. K. Kampouris and C. E. Banks, *RSC Advances*, 2012, **2**, 6672-6679.
23. A. Pendashteh, M. S. Rahmanifar, R. B. Kaner and M. F. Mousavi, *Chem. Commun.*, 2014, **50**, 1972-1975.
24. W. Zhou, X. Liu, Y. Sang, Z. Zhao, K. Zhou, H. Liu and S. Chen, *ACS Appl. Mater. Interfaces*, 2014, **6**, 4578-4586.
25. Y. Zhang, M. Ma, J. Yang, H. Su, W. Huang and X. Dong, *Nanoscale*, 2014, **6**, 4303-4308.

26. W. Zhou, D. Kong, X. Jia, C. Ding, C. Cheng and G. Wen, *J. Mater. Chem. A*, 2014, **2**, 6310-6315.
27. S. G. Krishnan, M. V. Reddy, M. Harilal, B. Vidyadharan, I. I. Misnon, M. H. A. Rahim, J. Ismail and R. Jose, *Electrochim. Acta*, 2015, **161**, 312-321.
28. M. R. Gao, S. Liu, J. Jiang, C. H. Cui, W. T. Yao and S. H. Yu, *J. Mater. Chem.*, 2010, **20**, 9355-9361.
29. Y. Zeng, R. Hao, B. Xing, Y. Hou and Z. Xu, *Chem. Commun.*, 2010, **46**, 3920-3922.
30. Y. Chen, H. Xia, L. Lu and J. Xue, *J. Mater. Chem.*, 2012, **22**, 5006-5012.
31. M. Sevilla, C. Salinas Martinez-de Lecea, T. Valdes-Solis, E. Morallon and A. B. Fuertes, *Phys. Chem. Chem. Phys.*, 2008, **10**, 1433-1442.
32. L. O'Neill, C. Johnston and P. S. Grant, *J. Power Sources*, 2015, **274**, 907-915.
33. H. Peng, Z. Mo, S. Liao, H. Liang, L. Yang, F. Luo, H. Song, Y. Zhong and B. Zhang, *Sci. Rep.*, 2013, **3**, 1765-1772.
34. L. Ji, L. Zhou, X. Bai, Y. Shao, G. Zhao, Y. Qu, C. Wang and Y. Li, *J. Mater. Chem.*, 2012, **22**, 15853-15862.
35. T. Sun, Z. Zhang, J. Xiao, C. Chen, F. Xiao, S. Wang and Y. Liu, *Sci. Rep.*, 2013, **3**, 2527-2533.
36. Y. Li, W. Zhou, H. Wang, L. Xie, Y. Liang, F. Wei, J. C. Idrobo, S. J. Pennycook and H. Dai, *Nat Nano*, 2012, **7**, 394-400.
37. O. N. Shebanova and P. Lazor, *J. Solid State Chem.*, 2003, **174**, 424-430.
38. O. N. Shebanova and P. Lazor, *J. Raman Spectrosc.*, 2003, **34**, 845-852.

39. E. Steven, W. R. Saleh, V. Lebedev, S. F. A. Acquah, V. Laukhin, R. G. Alamo and J. S. Brooks, *Nat. Commun.*, 2013, **4**, 2435-2442.
40. C. Long, T. Wei, J. Yan, L. Jiang and Z. Fan, *ACS Nano*, 2013, **7**, 11325-11332.
41. R. S. Nicholson and I. Shain, *Anal. Chem.*, 1964, **36**, 706-723.
42. R. S. Nicholson, *Anal. Chem.*, 1965, **37**, 1351-1355.
43. D. Liu, X. Wang, X. Wang, W. Tian, J. Liu, C. Zhi, D. He, Y. Bando and D. Golberg, *J. Mater. Chem. A*, 2013, **1**, 1952-1955.
44. T. Tsubota, M. Morita, N. Murakami and T. Ohno, *J. Power Sources*, 2014, **267**, 635-640.
45. S. Makino, Y. Shinohara, T. Ban, W. Shimizu, K. Takahashi, N. Imanishi and W. Sugimoto, *RSC Advances*, 2012, **2**, 12144-12147.
46. M. Hughes, M. S. P. Shaffer, A. C. Renouf, C. Singh, G. Z. Chen, D. J. Fray and A. H. Windle, *Adv. Mater.*, 2002, **14**, 382-385.
47. C. Du and N. Pan, *J. Power Sources*, 2006, **160**, 1487-1494.
48. C. He, S. Wu, N. Zhao, C. Shi, E. Liu and J. Li, *ACS Nano*, 2013, **7**, 4459-4469.
49. P. L. Taberna, S. Mitra, P. Poizot, P. Simon and J. M. Tarascon, *Nat. Mater.*, 2006, **5**, 567-573.
50. G. Zhou, D. W. Wang, F. Li, L. Zhang, N. Li, Z.-S. Wu, L. Wen, G. Q. Lu and H. M. Cheng, *Chem. Mater.*, 2010, **22**, 5306-5313.
51. E. Kang, Y. S. Jung, A. S. Cavanagh, G. H. Kim, S. M. George, A. C. Dillon, J. K. Kim and J. Lee, *Adv. Funct. Mater.*, 2011, **21**, 2430-2438.
52. X. Gu, L. Chen, S. Liu, H. Xu, J. Yang and Y. Qian, *J. Mater. Chem. A*, 2014, **2**, 3439-3444.
53. M. Zhi, A. Manivannan, F. Meng and N. Wu, *J. Power Sources*, 2012, **208**, 345-353.

54. X. Zhao, B. M. Sanchez, P. J. Dobson and P. S. Grant, *Nanoscale*, 2011, **3**, 839-855.

## TOC

$\text{Fe}_3\text{O}_4$  spherulites on carbon nanofibres (CNF) to form novel necklace structures were prepared by a facile method. The  $\text{Fe}_3\text{O}_4$ /CNF necklaces show superior performance for both supercapacitor and Li-ion battery applications.

